JOURNAL OF MATERIALS RESEARCH AND TECHNOLOGY 2023;23:5260–5269

Available online at www.sciencedirect.com

jmr&t Journal of Materials Research and Technology

journal homepage: www.elsevier.com/locate/jmrt

Original Article

# Sequence of phase transformations in metastable β Zr–12Nb alloy studied in situ by HEXRD and complementary techniques

A. Veverková [a,*], P. Harcuba [a], J. Veselý [a], P. Barriobero-Vila [c], P. Doležal [b], J. Pospíšil [b], K. Bartha [a], J. Šmilauerová [a], J. Kozlík [a], J. Stráský [a], M. Janeček [a]

[a] Department of Physics of Materials, Charles University, Ke Karlovu 5, 12116, Prague, Czech Republic
[b] Department of Condensed Matter Physics, Charles University, Ke Karlovu 5, 12116, Prague, Czech Republic
[c] Technical University of Catalonia (UPC), Department of Materials Science and Engineering, Eduard Maristany Av. 16, 08019 Barcelona, Spain

ARTICLE INFO

*Article history:*
Received 19 December 2022
Accepted 11 February 2023
Available online 18 February 2023

*Keywords:*
Metastable beta zirconium alloy
Phase transformations
High-energy X-ray diffraction
Transmission electron microscopy

ABSTRACT

Phase transformations in a metastable beta Zr–12Nb alloy were investigated by high-energy X-ray diffraction (HEXRD) measured simultaneously with thermal expansion in situ during linear heating from room temperature to 800 °C. Complementary in-situ methods of electrical resistance and differential scanning calorimetry, which were performed using the same heating conditions as in the HEXRD experiment, provided additional information on the transformation sequence occurring in the Zr–12Nb alloy. Two bcc phases with a different lattice parameter, $\beta_{Zr}$ and $\beta_{Nb}$, were observed in the investigated temperature range and identified using the phase diagram of the Zr–Nb system. In the initial solution-treated condition, metastable $\beta_{Zr}$ phase and athermal ω particles are present in the material. At about 300 °C, Nb-rich $\beta_{Nb}$ phase starts to form in the material and the original $\beta_{Zr}$ phase gradually disappears. Ex-situ observations of the microstructure using transmission electron microscopy revealed a cuboidal shape of the ω particles, which is related to a relatively large misfit between the ω and β phases. At 560 °C, ω solvus was observed, identified by an abrupt dissolution of ω particles which was followed by growth of the α phase.



## 1. Introduction

Zirconium has several physical properties which make it an attractive material for a wide range of applications. Due to its low thermal neutron capture cross-section, it is an essential construction material in the nuclear industry [1,2]. Zirconium also possesses a good corrosion resistance both in highly acidic and alkaline environments and therefore, it is frequently used in chemical industry [3]. Recently, Zr has been identified as a

* Corresponding author.
E-mail address: veverkova@karlov.mff.cuni.cz (A. Veverková).
https://doi.org/10.1016/j.jmrt.2023.02.076

promising material for biomedicine, as it is a biocompatible element, and its alloys generally exhibit good strength and a low elastic modulus [4]. As every pure metal, zirconium has a very low strength, and must be alloyed with other elements to improve its mechanical and corrosion properties. Traditionally, only low-alloyed zirconium alloys have been designed, studied and utilised extensively since the main application was nuclear industry and all alloying additions increase the total neutron capture cross-section. Therefore, designing zirconium alloys for nuclear industry is a trade-off between mechanical and neutron properties [1,5,6]. Zirconium is most commonly alloyed with Sn, Fe, Nb, or Mo. The first commercial zirconium alloys, Zircaloy-2 and Zircaloy-4, contain 1.5 wt% of Sn and low amounts of Fe and Cr [5,7,8]. Zr alloys E110 and M5 contain 1 wt% of Nb, which places them on the $\alpha/\alpha+\beta$ boundary in the Zr–Nb phase diagram [9]. Depending on the thermal treatment, the aforementioned alloys can contain small β phase particles enriched in the β-stabilising Nb [10–12]. The combined effect of Sn and Nb was used in more advanced alloys ZIRLO [13], E635 [14] and X5A [15]. Zr-Excel alloy with a more complex composition (Zr-3.5Sn-0.8Mo-0.8Nb-0.15Fe-0.13O) has been thoroughly studied [16,17] but never used in practice. In the chemical industry, the most frequently used Zr alloys are Zircadyne 702 and 705. Zircadyne 702 is commercially pure Zr and Zircadyne 705 is alloyed with Nb to increase its formability and strength [18].

However, low-alloyed Zr alloys do not fully utilize the well-known strengthening mechanisms of a multi-phase microstructure. The development of Zr alloys with a higher content of alloying elements opens new application possibilities due to their enhanced strength at room temperature and particularly at elevated temperatures. In nuclear industry applications, the adverse effect of increased neutron capture cross-section can be compensated by the increased strength due to precipitation strengthening. In other words, higher strength enables developing a subtler design of internal components of the nuclear reactor. This, in turn, results in a lower weight, reduced production costs and to a reduced total neutron capture cross-section of the components.

Zirconium belongs to the same group of periodic table of elements as titanium; the phases and phase transformations observed in alloys based on these elements are similar.

In literature, there are numerous studies of metastable β-Ti alloys [19–24]; several Ti alloys with unique mechanical properties were developed and are extensively used in the aerospace industry [25]. In comparison, studies of zirconium alloys with a higher amount of alloying additions have been rather scarce. Apart from investigations of metastable β-Zr alloys in the 70's and 80's [26,27], there is only limited recent research on phase transformations, microstructure changes and mechanical properties, Ref. [28], and corrosion performance, Ref. [29]. Near β-type Zr alloys were found to possess a high strength and a low elastic modulus which is an ideal combination for biomedical applications [30,31]. Zr has also significantly lower magnetic susceptibility than other metals used for hard-tissue replacements (Fe and Ti), which leads to less problematic magnetic resonance imaging of patients with Zr implants. With this attribute in mind, alloys from the Zr–Mo and Zr–Nb system (including Zr-12Nb alloy studied in this paper) were developed and investigated [32–34].

To our knowledge, no detailed study of phase transformations and their sequence during heating of metastable β-Zr alloys has beed reported in the literature. However, a full understanding of phase transformations is essential for the development and utilisation of metastable β-Zr alloys as high-strength materials. In this study, we investigated phase transformations in a simple binary Zr–12Nb (in wt %) alloy whose composition was selected based on the analogy with the thoroughly investigated Ti–15Mo (wt %) alloy [19,20,35–37]. When the binary phase diagrams of the Zr–Nb and Ti–Mo systems are compared (see Refs. [38,39], respectively), it is clear that the effect of Nb on the phase transformations in Zr is qualitatively similar to the effect of Mo in Ti. The content of 12 wt% Nb in the studied Zr alloy was selected to achieve the same degree of β phase stabilization as in the Ti–15Mo alloy.

The transformation sequence in the Ti–15Mo alloy during linear heating is thoroughly described in Refs. [19,37]. We will introduce it very briefly here for the sake of clarity. After quenching from a temperature above the β-transus temperature, Ti–15Mo (as a metastable β alloy) does not contain any α phase nor any martensitic α′ or α″ phases. However, metastable $\omega_{ath}$ (athermal) phase is formed during quenching by a diffusionless transformation. The mechanism of $\omega_{ath}$ formation corresponds to a shift of two neighbouring $(111)_\beta$ planes along the body diagonal of the cubic cell to their intermediate position, while one $(111)_\beta$ plane between two pairs of collapsed planes is left unchanged [40,41]. It has been shown that the collapse can be only partial, which results in a trigonal symmetry of the ω phase [42]. Since there are four crystallographically equivalent sets of $\{111\}_\beta$ planes, there are also four possible crystallographic orientations (families) of the ω lattice. Due to the mechanism of ω formation there is a specific crystallographic orientation between the ω and β lattices: $(0001)_\omega \parallel (111)_\beta, [11\bar{2}0]_\omega \parallel [011]_\beta$. The lattice misfits are defined as the relative differences of the lattice parameters of the ω phase from their "ideal" values:

$$a_\omega^{(id)} = a_\beta\sqrt{2}, c_\omega^{(id)} = a_\beta\sqrt{3}\Big/2,$$

$$f_a = \left(a_\omega - a_\omega^{(id)}\right)/a_\omega^{(id)}, f_c = \left(c_\omega - c_\omega^{(id)}\right)/c_\omega^{(id)}, \quad (1)$$

where $a_\beta$ is the lattice parameter of the body-centered cubic β phase and $a_\omega$, $c_\omega$ are lattice parameters of the hexagonal ω phase. The superscript (id) denotes the "ideal" values following from the crystallographic orientation between ω and β lattices stated above.

During ageing at intermediate temperatures (250 °C–450 °C), ω particles stabilize chemically by rejecting β-stabilising elements into the surrounding β matrix. This phase is referred to as the $\omega_{iso}$ (isothermal) phase. At approximately 560 °C, the ω phase dissolves abruptly and the α phase starts to precipitate. The maximum volume fraction of the α phase is reached around 600 °C and then decreases as the temperature approaches the β transus temperature. Above the β transus, α phase is no longer present and the material consists of a pure β phase [19].

In this work, phase transformations in the Zr–12Nb alloy were studied by high-energy X-ray diffraction (HEXRD) in situ during linear heating. The method has already been used for

investigation of phase transformations in titanium alloys [22–24,35]. However, to our knowledge, metastable β-Zr alloys have never been studied using HEXRD. The HEXRD measurement was complemented by dilatometry (measured simultaneously with X-ray diffraction), differential scanning calorimetry (DSC) and electrical resistance. Based on the obtained results, several conditions were chosen for post-mortem microstructure observations by transmission electron microscopy (TEM). The results are compared with results achieved for the analogous Ti15Mo alloy [36].

## 2. Methods

The alloy used in this study was arc melted at UJP Praha a. s. in pure He atmosphere. The material was homogenised in vacuum at 1400 °C for 2 h, processed by rotary swaging and solution treated at 1000 °C for 2 h with subsequent quenching to water (hereafter referred to as the initial material).

The phase transformations and the evolution of individual phases was investigated by high-energy X-ray diffraction (HEXRD) at P07-HEMS beamline of PETRA III (Deutsches Elektronen-Synchrotron) [43]. A modified dilatometer Bähr 805A/D was used to heat the samples in an inert He atmosphere and record the thermal expansion simultaneously [44]. A sample of a cylindrical shape with the diameter of 4.5 mm and the length of approximately 10 mm was used for the measurement, which was carried out in transmission mode with the primary beam perpendicular to the length of the specimen. The wavelength of the X-ray beam was 0.14235 Å. Data acquisition was performed in situ during linear heating from room temperature (RT) to 800 °C using the heating rate of 5 °C/min. The patterns of entire Debye-Scherrer rings were recorded by a PerkinElmer XRD 1621 image plate detector. One pattern consisted of 15 frames, each with the acquisition time of 1 s. The distance between the detector and the sample was about 1580 mm and the beam size was 0.7 mm × 0.7 mm. The obtained Debye-Scherrer rings were processed by the program fit2D to get the integrated 2θ profiles [45]. Subsequently, the profiles were refined using the Rietveld method in the FullProf program [46].

Electrical resistance of the material was measured using the same heating conditions as those employed during the HEXRD experiment, i.e. linear heating with the heating rate of 5 °C/min up to 800 °C. Electrical resistance was measured by a four-point method under an inert Ar atmosphere using a home-made apparatus which is able to achieve a relative error of the order of $10^{-5}$; the details can be found in Ref. [36]. The electrical resistance was normalized to the value at RT, i.e. $R/R_{RT;}$ therefore, it can be regarded as the relative resistance with respect to room temperature.

The in-situ experiments were complemented by differential scanning calorimetry (DSC) using Netzsch DSC 404C Pegasus calorimeter. The sample was heated with the same heating rate of 5 °C/min up to 800 °C.

Microstructure observation for selected conditions was done ex situ in a JEOL 2200FS transmission electron microscope (TEM) operated at 200 keV. For this purpose, samples of the initial material were encapsulated in a quartz tube filled with Ar, linearly heated using the same heating rate of 5 °C/min up to the desired temperature and quenched into water. The selected temperatures for microstructure observation were 400 °C, 500 °C, and 600 °C. Subsequently, the samples for TEM analysis were thinned by mechanical grinding to the thickness of approx. 120 μm. The first polishing step was electropolishing in Tenupol-5 (Struers) in a solution of $HClO_4$, butanol and methanol. The electropolishing was performed at −20 °C using the voltage of 20 V. The final polishing step was ion milling using PIPS (Gatan) operating at 5 kV; for the last 30 min, the accelerating voltage was reduced to 3 kV to achieve a smooth surface of the TEM lamella.

## 3. Results and discussion

### 3.1. *In-situ high-energy X-ray diffraction (HEXRD)*

Fig. 1 shows the evolution of diffracted intensity measured by HEXRD during linear heating with the heating rate of 5 °C/min from RT to 800 °C. The horizontal axis represents the interplanar distance, while the temperature is shown on the vertical axis. The colour represents the diffracted intensity in a logarithmic scale. The lower part of the plot shows the calculated positions of the β, ω and α diffraction peaks at RT, 350 °C and 650 °C, respectively. In Fig. 1, peaks arising from the three phases can be clearly distinguished. The strongest peaks which extend through the whole temperature range correspond to the β phase. Peaks arising from the presence of the ω phase can be identified as much weaker, broader maxima. Up to approximately 300 °C, the character of the diffraction pattern does not change significantly. When the temperature is further increased, the ω phase peaks sharpen and increase in intensity, while the β peaks widen. Concurrently, a slight shift of both β and ω peaks (associated with lattice parameters changes) is visible in Fig. 1. At 560 °C, an abrupt change of the diffraction pattern is observed; the ω peaks disappear, which corresponds to the dissolution of ω particles at the ω-solvus

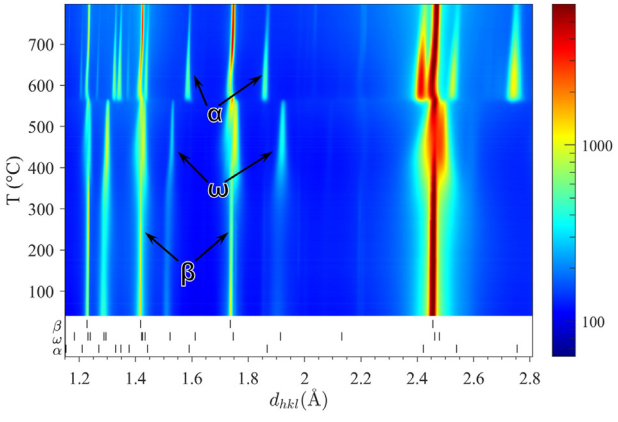


**Fig. 1 – Evolution of the Zr–12Nb diffraction pattern during linear heating from RT to 800 °C with the heating rate of 5 °C/min. The interplanar distance $d_{hkl}$ is shown on the horizontal axis, the vertical axis represents the temperature. The colour represents the diffracted intensity in a logarithmic scale. The lower part of the plot shows the positions of the β, ω, and α phase peaks.**

temperature. The dissolution of the ω phase at the ω solvus is not governed by diffusion and therefore, the temperature of the ω solvus is independent of the heating rate [20]. As the ω peaks disappear, they are replaced by the α phase peaks. Upon closer inspection, there is a narrow temperature range around 560 °C in which the ω and α phases coexist. As the temperature approaches the upper limit for the HEXRD experiment (800 °C), α maxima gradually weaken; however, a complete dissolution of the α phase was not observed.

Representative HEXRD patterns taken at RT, 400 °C, 540 °C and 580 °C are shown in Fig. 2. Note that all body-centred cubic (bcc) peaks are referred to as the β phase in Fig. 2, disregarding the distinction between $\beta_{Zr}$ and $\beta_{Nb}$ phases discussed further in the text. The initial condition of the Zr–12Nb alloy consists of the β phase and $\omega_{ath}$ particles (see the blue line in Fig. 2a). The β peaks are narrow and strong (e.g. at $d_{hkl} \approx 1.42$ Å, 1.74 Å or 2.46 Å), while the presence of the ω phase is evidenced by typical broad peaks of a lower intensity ($d_{hkl} \approx 1.29$ Å, 1.51 Å, 1.90 Å). This result is consistent with analysis of Zr–Nb alloys reported in Refs. [33,34]. Since all β peaks coincide with one or more ω peaks, the tails of the β maxima are unusually broad. In the diffraction pattern obtained for the temperature of 400 °C (the red line in Fig. 2a), an increase of the intensity of the ω peaks can be observed. The higher intensity of ω peaks with positions close to the β peaks results in the formation of pronounced shoulders of these β peaks, see e.g. the $(101)_\beta$ maximum at 2.46 Å. The comparison of diffraction patterns taken slightly below and above the ω-solvus (560 °C) is displayed in Fig. 2b. Below the ω-solvus (see the blue line in Fig. 2b which represents a pattern obtained at 540 °C), intense ω peaks can be observed. Interestingly, there is a very small amount of the α phase in the material, as evidenced by a very shallow $(10.2)_\alpha$ peak at $d_{hkl} \approx 1.86$ Å, for example. Above 560 °C, all ω peaks disappear and peaks of the α phase rapidly increase in their intensity (e.g. $d_{hkl} \approx 1.59$ Å, 1.86 Å, 2.74 Å, see the red line in Fig. 2b, representing a pattern at 580 °C).

The HEXRD data were refined using the Rietveld method which yielded the lattice parameters of individual phases, their weight fractions and molar volumes. As opposed to the typical transformation sequence in metastable β titanium alloys, in which a single bcc β phase can be detected in the whole temperature range between RT and the β-transus [19,22–24], the fitting of the Zr–12Nb diffraction patterns revealed the successive presence of two types of bcc phase with different lattice parameters and a short temperature interval of coexistence. This is best visible in the evolution of the peak at $d_{hkl} \approx 1.74$ Å and its deconvolution into individual phases as shown in Fig. 3. The identification of the two bcc phases follows from the phase diagram of the Zr–Nb system

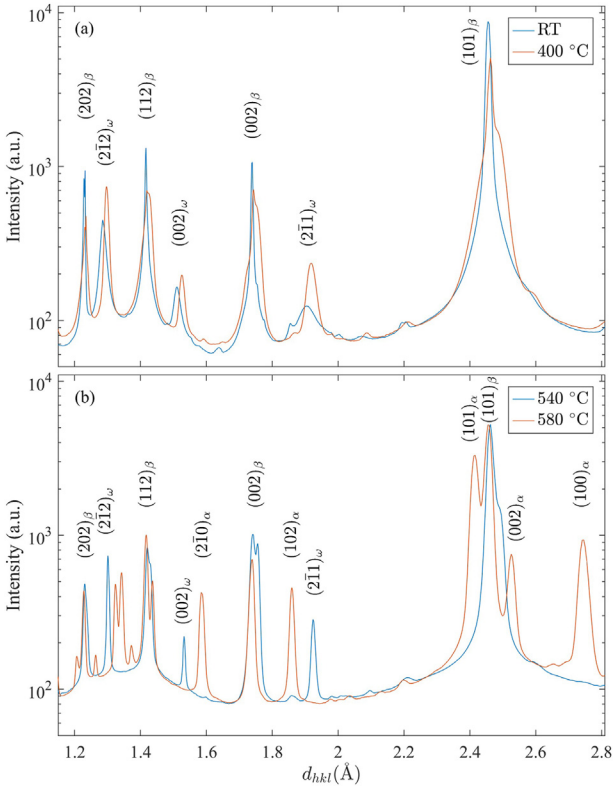


**Fig. 2 – HERXD patterns acquired at RT, 400 °C, 540 °C and 580 °C. Selected peaks are indexed.**

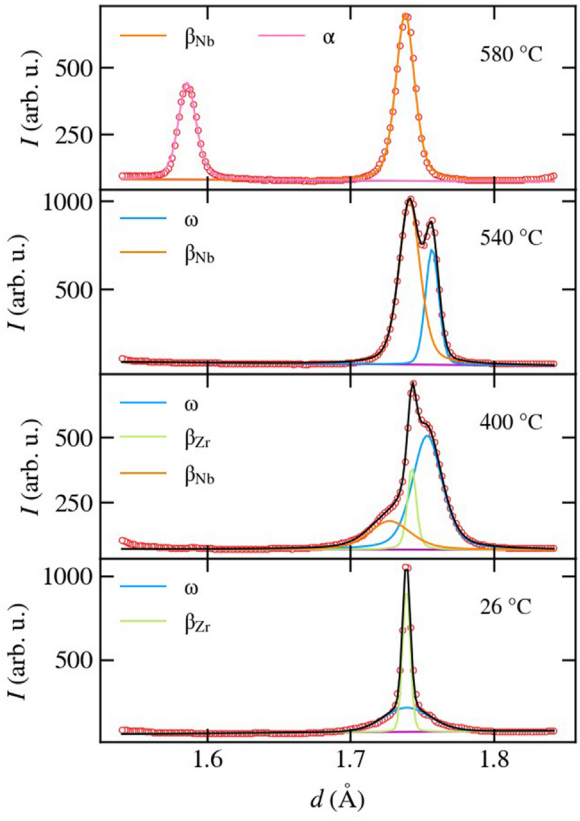


**Fig. 3 – Evolution of the peak at $d_{hkl} \approx 1.74$ Å (indexed as $(002)_\beta$ in Fig. 2). Red circles represent measured data, coloured lines are fitted peaks of individual phases. At room temperature (the plot at the bottom), the peak is fitted by $\beta_{Zr}$ and ω phases. At 400 °C, the intensity of the ω peak increased, while the $\beta_{Zr}$ peak is weaker and a new $\beta_{Nb}$ can be observed. At 540 °C, the $\beta_{Zr}$ phase is no longer present in the sample and there is only a mixture of $\beta_{Nb}$ and ω phases. Above the ω-solvus, here at 580 °C (the top plot), the material consists of α and $\beta_{Nb}$.**

displayed in Fig. 4, which was calculated in the Thermo-Calc software (TTZR1: Zr-based alloys database v1.1). The composition of the studied alloy Zr–12Nb is indicated in the phase diagram by the blue vertical line. When the Zr–12Nb alloy is rapidly cooled to room temperature, it contains the quenched-in $\beta_{Zr}$ phase in which metastable $\omega_{ath}$ particles form to release some of the strain energy related to the high-temperature $\beta_{Zr}$ phase being "frozen" in a thermodynamically metastable state. The lower plot in Fig. 3 demonstrates that the phase composition of the alloy at RT is $\beta_{Zr} + \omega$. As the temperature is subsequently increased into the range in which diffusion operates effectively, ω phase particles start to grow by a diffusion-assisted process accompanied by the rejection of Nb into the surrounding matrix. Driven both by the excess Nb and the fact that it is far from the thermodynamic equilibrium, the $\beta_{Zr}$ phase starts to decompose and regions of Nb-rich $\beta_{Nb}$ phase form according to the phase diagram (Fig. 4). The plot for 400 °C in Fig. 3 shows a strong ω maximum, much weaker $\beta_{Zr}$ peak, and a shallow and broad $\beta_{Nb}$ peak. The peak arising from $\beta_{Nb}$ is found at a lower $d_{hkl}$, which is consistent with the fact that Nb decreases the lattice parameter of the bcc phase [22,47]. The conspicuous broadening and a slight asymmetry of the $\beta_{Nb}$ peak (due to which the fitting of this phase was problematic in the early stages of its evolution) is probably caused by a concentration gradient of Nb and/or elastic strains in the $\beta_{Nb}$ phase. On the other hand, the peaks corresponding to the original $\beta_{Zr}$ phase are sharp despite their decreasing intensity (see the green lines in Fig. 3). Therefore, there are no strong chemical gradients in the $\beta_{Zr}$ phase as opposed to $\beta_{Nb}$.

Eventually, $\beta_{Zr}$ disappears completely and the material is composed of a mixture of $\beta_{Nb}$ and ω phases, see the part of diffraction pattern at 540 °C in Fig. 3. Note that the $\beta_{Nb}$ peak shifts into the position of the original $\beta_{Zr}$ peak, which is due to changing Nb content in the β phase discussed below. As the temperature increases above the ω solvus, ω particles dissolve and the alloy system approaches the thermodynamically stable $\alpha_{Zr}+\beta_{Nb}$ phase composition, see the phase diagram in Fig. 4 and the upper plot in Fig. 3.

The evolution of weight fractions of phases during linear heating is shown in Fig. 5 by coloured symbols. The weight fraction is analogous to the volume fraction; the two parameters would be identical if all phases in the material had the same density. However, the difference between densities of individual phases is of the order of several percent, so the weight and volume fractions can be regarded as interchangeable terms. The diffraction data suffer from poor statistics due to relatively low number of irradiated grains. Therefore, the absolute error of the weight fraction values is difficult to estimate and can be quite large. All small steps in the weight fraction evolution, especially at temperatures where a new phase was included into the fitting parameters (e.g. at 350 °C and 560 °C where the first indications of $\beta_{Nb}$ and α phases, respectively, became apparent in the diffraction patterns), are fitting artifacts. However, the general trends of the curves are correct.

Fig. 5 also displays the evolution of relative electrical resistance, denoted by the black line. Electrical resistance is sensitive to microstructure changes and phase transformations. We emphasize that the black curve in Fig. 5 shows the raw electrical resistance data, only normalized to the resistance value at RT; no smoothing or any mathematical operation was performed. According to Matthiessen's rule, the total resistance of a sample can be approximated by the sum of two terms: $\rho_{tot}(T) = \rho_0 + \rho_h(T)$. The temperature-independent component $\rho_0$ is the contribution of impurities and irregularities in the periodicity of the crystal lattice (e.g. foreign atoms, phases and their interfaces, or strain fields). The temperature-dependent component $\rho_h(T)$ denotes the resistance of the pure host metal which is governed mainly by the scattering of conduction electrons on thermal vibrations (phonon scattering) [48]. In

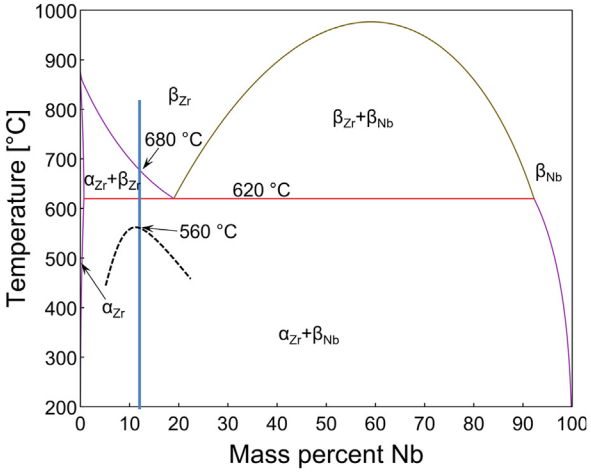


**Fig. 4 – Zr–Nb phase diagram calculated in the Thermo-Calc software. The blue vertical line denotes the chemical composition of the Zr-12Nb alloy. The dashed line shows schematically the variation of the ω solvus temperature; the value 560 °C for 12 wt %Nb was determined in this paper. The theoretical eutectoid and β-transus temperatures (620 °C and 680 °C, respectively) are also indicated.**

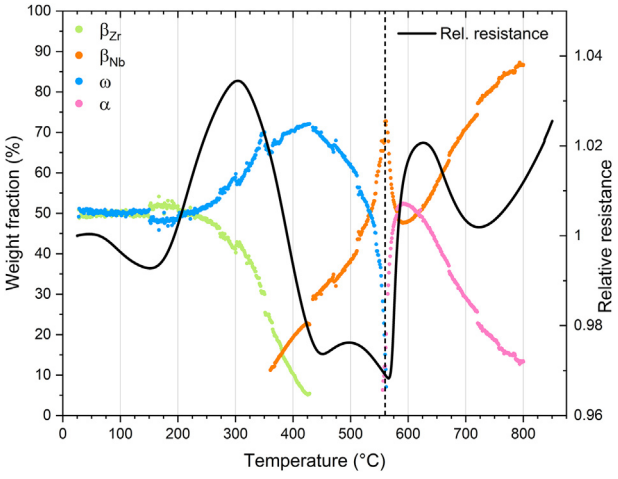


**Fig. 5 – Evolution of weight fractions of individual phases in the Zr–12Nb alloy during linear heating (represented by coloured symbols). The black line shows the evolution of relative electrical resistance ($R/R_{RT}$). The dashed vertical line denotes the ω solvus temperature at approximately 560 °C.**

an alloy heated from RT to 850 °C, the phonon scattering is responsible for an increase in resistance by approximately 20% [49]. When the resistance decreases during linear heating, it means that some process in the material (microstructure change or phase transformation) which decreases the resistance is stronger than the phonon contribution arising from the temperature increase. On the other hand, when the resistance curve increases, it may mean that it is only due to the phonon scattering, or that some process has either a weaker opposing influence or contributes to it. The phonon contribution can be roughly estimated from the slope of the resistance curve at the highest temperatures (ideally above the β transus, which could not be reliably identified by our experiments), where there are no significant changes in the microstructure.

The evolution of lattice parameters evaluated from fitting of the diffraction patterns is shown in Fig. 6. The small steps at temperatures where a phase was either added or removed from the fitting parameters (e.g. around 350 °C and 560 °C where the $\beta_{Nb}$ and α phase could be first identified in the diffraction pattern, respectively) are only fitting artifacts.

Fig. 7 shows the dependence of molar volumes of ω, $\beta_{Zr}$, $\beta_{Nb}$ and α phases on temperature. The molar volume is the volume of the unit cell divided by the number of atoms per unit cell and multiplied by Avogadro constant. In other words, it is the volume which would be occupied by 1 mol of atoms ordered in a given crystallographic lattice with given lattice parameters. Similar to the curves representing weight fractions and lattice parameters (Figs. 5 and 6, respectively), small jumps in the molar volume curves (coloured lines in Fig. 7) are only artifacts of data reduction; however, the trends are correct and the values are reliable. The graph also shows relative thermal expansion, which provides complementary information on the sample length changes.

### 3.2. *Ex-situ observation of the microstructure*

The weight fractions, lattice parameters or molar volumes of individual phases evaluated from HEXRD provide no information on the sizes of ω and α particles, nor on the real microstructure of the sample. Therefore, the microstructure of the Zr–12Nb alloy in the initial solution-treated condition and after linear heating to selected temperatures (400 °C, 500 °C and 600 °C) was studied by TEM, see Fig. 8. It should be noted that the TEM images are taken ex situ, i.e. the material was quenched to room temperature after linear heating to the selected temperature. Consequently, the observed microstructure may differ from the one at high temperatures, as some phase transformations may occur during quenching. However, the ex-situ approach is actually more appropriate than an in-situ TEM experiment, because the diffusional phase transitions can significantly differ in a thin foil and in bulk material. As a result, the temperature ranges and kinetics of some transformations will be shifted, while other transformation will not be observed at all in the thin foil [50].

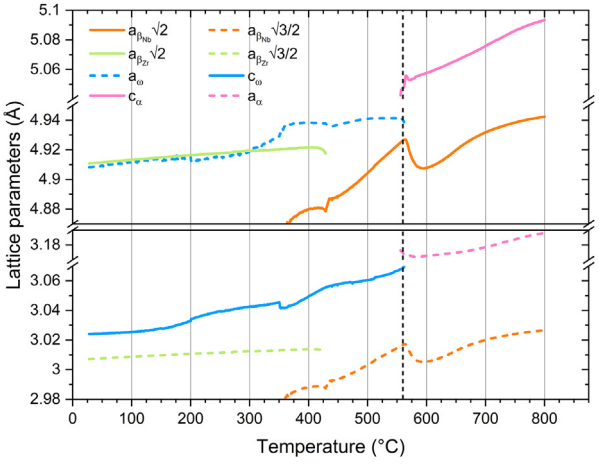


**Fig. 6 – Evolution of lattice parameters of individual phases during linear heating. The lattice parameter $a_{\beta}$ is plotted to show the lattice misfit between ω and β phases as defined by Eq. (1), i.e. multiplied by $\sqrt{2}$ and $\sqrt{3}/2$.**

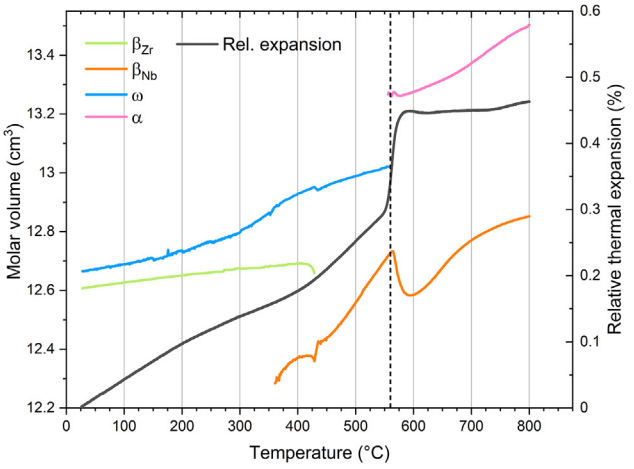


**Fig. 7 – Evolution of the molar volume of phases in Zr–12Nb during linear heating, denoted by coloured curves. The relative thermal expansion of the sample (black curve) is plotted in the same graph.**

The dark-field (DF) image of the initial material is shown in Fig. 8a. The bright spots correspond to very small $\omega_{ath}$ particles with sizes in the range of nanometres. After heating to 400 °C (i.e. the temperature at which the weight fraction of the ω phase is the highest and a coexistence of $\beta_{Zr}$ and $\beta_{Nb}$ phases was determined, see Fig. 5, a slight increase of the size of ω particles can be observed, see Fig. 8b. However, a TEM observation cannot be used to assess the volume fraction, as the observed density of particles depends on the thickness of the TEM foil and on the fraction of particles fulfilling the diffraction condition. For example, DF images in Fig. 8 a–c display only one fourth of the total number of ω particles, as there are four crystallographic "families" of ω particles and only one of them is selected for imaging. Heating to 500 °C results in significant coarsening of ω particles, see Fig. 8c. The size of ω particles is approximately 50 nm and their shape is cuboidal (cf. ellipsoidal ω particles in Ti–15Mo [20]). Fig. 8d and e show the BF and DF images, respectively, of a sample heated to 600 °C. Small, elongated particles of the α phase are visible in the BF image, Fig. 8d. At the temperature of 600 °C, ω phase is completely dissolved, as evidenced by HEXRD results (see e.g. Fig. 5). The ω particles observed in the images Fig. 8d and e are

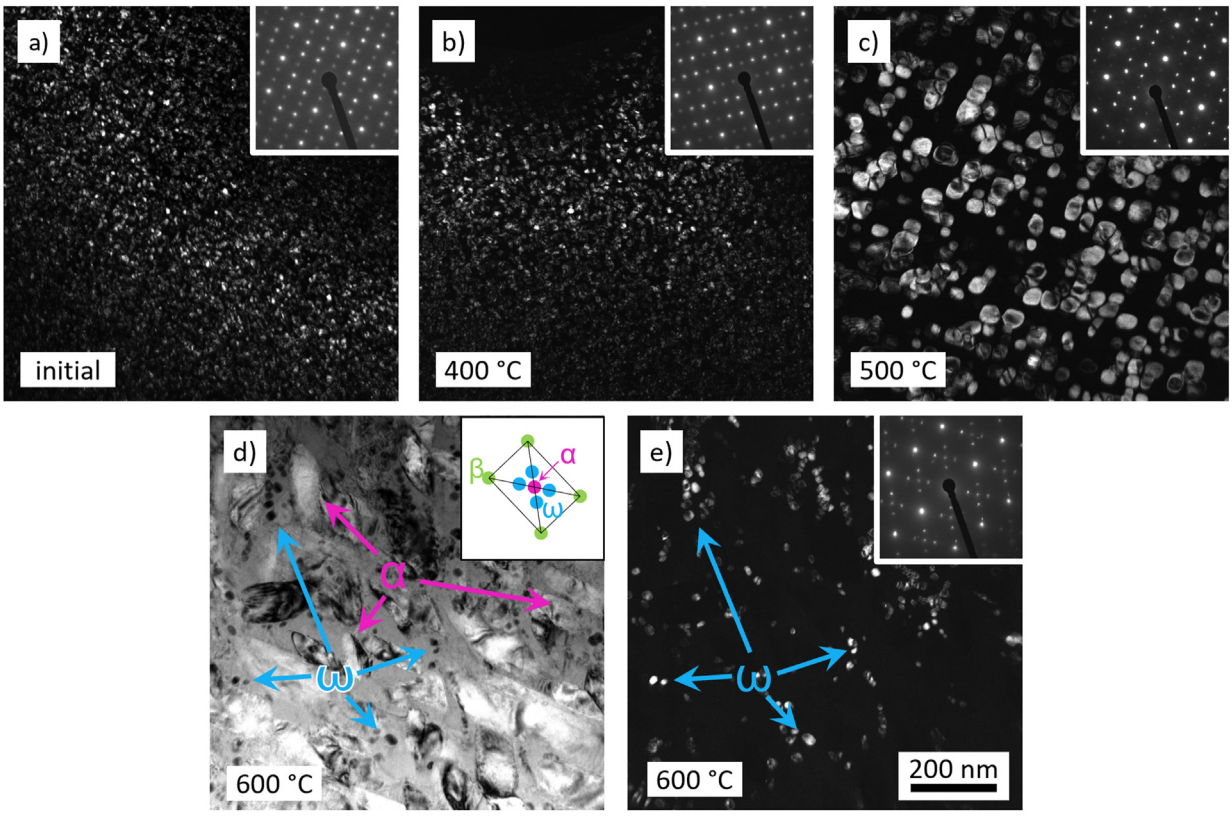


**Fig. 8 – TEM micrographs of a) initial (solution treated) condition of the Zr–12Nb alloy, and the conditions obtained by linear heating (5 °C/min) to a selected temperature and quenching: b) 400 °C, c) 500 °C, d) and e) 600 °C. Panels a), b), c) and e) show DF images with the corresponding selected area electron diffraction (SAED) patterns, while d) is a BF image. d) and e) show the same region of the specimen. Blue arrows indicate $\omega_{ath}$ particles formed in the sample during quenching, magenta arrows show selected α particles. The inset in d) indicates the indexation of the SAED pattern, the orientation of the sample was $(110)_\beta$ perpendicular to the electron beam. The scale of all images is identical and is indicated in panel e).**

athermal ω ($\omega_{ath}$) which were formed in the $\beta_{Nb}$ phase during quenching from 600 °C. Similar effect of $\omega_{ath}$ formation during quenching from a temperature at which the β and α phases coexisted, while the ω phase was not present, was observed in Ref. [20].

### 3.3. *Comparison of dilatometry, electrical resistance and differential scanning calorimetry (DSC)*

Fig. 9 shows a comparison of in-situ measurements of electrical resistance, dilatometry and DSC. The derivatives of resistance and thermal expansion are shown, as these can be directly correlated to the DSC curve.

The DSC curve (red line in Fig. 9) is qualitatively similar to those measured for Ti–15Mo and Ti-LCB (Ti-6.8Mo-4.5Fe-1.5Al) [51]. Several processes can be distinguished on the DSC curve. In the temperature range of approximately 150 °C–450 °C, two broad exothermic bumps can be observed. The first one (150 °C–270 °C) was, in the case of Ti alloys, attributed to the start of irreversible (i.e. with diffusion already playing a role) dissolution of $\omega_{ath}$ [36,51]. In weight fraction data from the HEXRD experiment (Fig. 5), a small bump is observed in this temperature range. However, due to the low reliability of the weight fraction data, we consider this effect inconclusive. Another explanation for the first exothermic bump in the DSC curve can be the release of elastic strains in the metastable $\beta_{Zr}$ phase which is in a metastable state after quenching. The second exothermic bump on the DSC curve (approx. 270 °C–450 °C) coincides with the formation of the $\beta_{Nb}$ phase and concurrent increase in the ω weight fraction, see Fig. 5. Note that the $\beta_{Nb}$ starts to form at a lower temperature than that corresponding to the beginning of the orange line in Fig. 5. However, its amount is below the detection limit of the HEXRD method. In the temperature range from approximately 450 °C to 560 °C, the DSC signal deviates in the endothermic sense, which can be attributed to the dissolution of the ω phase, see Fig. 5. At 560 °C, the onset of a sharp exothermic peak is observed which is connected to α phase precipitation above the ω solvus.

### 3.4. *The transformation sequence in Zr–12Nb during linear heating*

From Fig. 5 it follows that at RT, the fractions of the $\beta_{Zr}$ and $\omega_{ath}$ phases (in green and blue, respectively) are both close to 50% and remain almost constant to approximately 200 °C. The

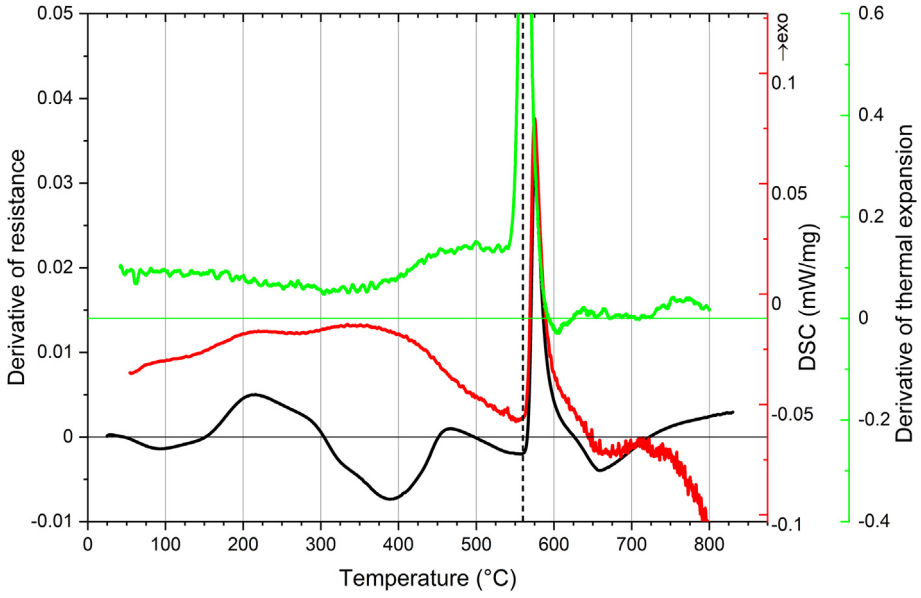


**Fig. 9 – The comparison of in-situ measurements of electrical resistance, thermal expansion and DSC. The derivatives of resistance and thermal expansion (black and green curve, respectively) are shown in the graph. The black and green horizontal lines denote the zero value of the derivatives.**

electrical resistance in this interval shows first a slight increase followed by a decrease. In metastable β-Ti alloys, the electric resistance decreases substantially above RT which was explained by partial dissolution of $\omega_{ath}$ particles into the β matrix and proven by in situ neutron diffraction [19]. On the other hand, the dissolution of $\omega_{ath}$ is rather limited in the Zr-12Nb alloy, as evidenced by the almost constant weight fraction of ω phase in Fig. 5 (blue dots). The slight decrease of electric resistance can be probably explained by partial release of elastic strains in the $\beta_{Zr}$ matrix due to either increasing temperature or the dissolution of a very small amount of ω phase, which cannot be clearly identified by X-ray diffraction.

The increase in electrical resistance between 150 °C and 250 °C is most likely caused only by phonon scattering, as no significant changes in the phase composition were detected by HEXRD. Starting from 250 °C, the weight fraction of the ω phase increases at the expense of the $\beta_{Zr}$ phase and the rising trend of resistance slows down (i.e. the effect of microstructure changes opposes the effect of phonon scattering). Therefore, the growth of ω particles causes a decrease in the resistance of the sample since a higher fraction of the ω phase is more effective in relieving the strains in the β phase related to the bcc structure being "frozen" far from the region of its thermodynamical stability. Another factor which may contribute to the decrease of electrical resistance can be the change of the character of the β/ω interfaces from coherent to semicoherent. The change of the interface character is most likely the reason for an increasing misfit between the ω and β phases which starts around 300 °C, see the deviation of blue dashed line from the green line in Fig. 6, i.e. at the temperature at which the electrical resistance begins to decrease, see Fig. 5. Around 350 °C, the second bcc β phase ($\beta_{Nb}$) was detected in the diffraction patterns. However, it started to form in the material earlier, but its volume fraction was below the detection limit of the method (less than approx. 10%). We estimate the real onset of $\beta_{Nb}$ to approximately 300 °C, where a deviation of the $a_\omega$ lattice parameter from its "ideal" value occurs, cf. Eq. (1) and Fig. 6, where the blue dotted line ($a_\omega$) deviates from the green one ($a_\beta\sqrt{2}$). Furthermore, the DSC curve also shows an exothermic bump starting slightly below 300 °C, which can be attributed to $\beta_{Nb}$ formation in the material, see the red curve Fig. 9.

After the original bcc phase, $\beta_{Zr}$, disappears at around 450 °C, a significant increase of the ω particle size is observed by TEM, see Fig. 8c. Note that the growth of ω particles coincides with a decrease in its weight fraction, see Fig. 5. Concurrently with the disappearance of the $\beta_{Zr}$ phase, a slight increase followed by another decrease can be observed in the electrical resistance curve. This is an interesting phenomenon which clearly indicated that there are two separate microstructural processes in the temperature range between 300 °C and 560 °C. Corresponding electrical resistance curve obtained for the Ti–15Mo alloy did not exhibit such clear distinction of the two processes, although a slight change in the downward slope of the resistance curve was detected [20,36]. The slight increase of electrical resistance around 450 °C is observed because the effect of microstructure changes which decrease the resistance (i.e. the dissolution of the ω phase) is weaker than the rising trend of phonon scattering. Gradually, the rate of the ω phase dissolution increases, until the influence of disappearing ω/β interfaces outweighs the phonon scattering and a decrease in electrical resistance is observed in the range from 500 °C to 560 °C; see the steeply declining curve of ω phase weight fraction in Fig. 5. In the range of 450 °C–560 °C, the lattice parameter of the $\beta_{Nb}$ increases more rapidly than what would result only from thermal dilatation, see Fig. 6. The consequent increase of the volume of $\beta_{Nb}$ unit cell is manifested in the dilatometric curve as a slightly steeper slope, see Fig. 7. Note that in this temperature range, the ω phase, which has a large molar volume, dissolves into $\beta_{Nb}$ with a smaller molar volume. This effect

opposes the increase in the sample length. Therefore, the effect of increasing $\beta_{Nb}$ lattice parameter needs to be truly strong as it is indeed manifested in the dilatometric curve. The $\beta_{Nb}$ lattice parameter growth can be explained by a lower average Nb content; as the ω phase (which is lean in Nb) dissolves, Nb contained in the $\beta_{Nb}$ matrix diffuses to the regions of former ω.

The cuboidal shape of ω particles (see Fig. 8c) is related to a large lattice misfit between the ω and $\beta_{Nb}$ phases [52], cf. the blue and orange lines in Fig. 6. The misfit as defined by Eq. (1) is about 2%.

At 560 °C, the ω solvus temperature is observed, i.e. all ω particles still present in the material abruptly dissolve and the α phase starts to precipitate. This phenomenon is manifested by a sharp minimum of the electric resistance. According to the phase diagram in Fig. 4, a relatively large fraction of the α phase would be observed in thermodynamic equilibrium at this temperature. The diffusion in this temperature range (i.e. between the ω solvus at 560 °C and the eutectoid temperature 620 °C, which coincides with a local maximum in the electrical resistance curve) is quite fast, and consequently, the precipitation and growth of α phase particles is very rapid. Combined effects of the phonon contribution and the rapid growth of α result in a steep increase of the electric resistance (see Fig. 5). The rapid growth of α phase is also clearly visible in all other in-situ methods. The thermal expansion of the sample significantly increases, since a large amount of α phase with a larger molar volume than the $\beta_{Nb}$ matrix forms in the material (see Fig. 7). Similarly, DSC detects a sharp exothermic peak with an onset at 560 °C due to α precipitation, see the red curve in Fig. 9. Concurrently, the lattice parameter of the $\beta_{Nb}$ phase decreases, see Fig. 6, due to increasing Nb content which is rejected from the newly formed α phase (Nb decreases the lattice parameter of bcc β phase [33,47]).

Above the eutectoid temperature, the α phase begins to dissolve. This is caused by the fact that below the eutectoid temperature, the equilibrium volume fraction of the α phase is larger than that of the $\beta_{Nb}$ phase (almost 9:1 according to the calculated phase diagram in Fig. 4). As the temperature rises above the eutectoid one, the situation is reversed; the equilibrium β fraction is larger than that of α. As the temperature approaches the β transus, the fraction of the α phase further decreases. Note that above the eutectoid temperature, it would be formally correct to call the $\beta_{Nb}$ phase (which started to form around 300 °C and its weight fraction gradually increased until it fully replaced the initial quenched-in $\beta_{Zr}$ phase) $\beta_{Zr}$ again, according to the phase diagram in Fig. 4. However, the evolution of lattice parameters or any other experiments do not indicate any structural change. Because renaming the bcc phase above the eutectoid temperature would bring more confusion than clarity, we will continue to call it $\beta_{Nb}$ (or just β). The theoretical value of the eutectoid temperature is 620 °C, see Fig. 4. In reality, it is shifted to a lower temperature; the fast dissolution of the α phase begins slightly below 600 °C, as evidenced by the weight fraction evaluated from HEXRD data, see the magenta curve in Fig. 5. This shift can be caused by content of impurities, namely oxygen, in the material which is not accounted for in the Zr-Nb phase diagram. Near the eutectoid temperature, a change of the slope in the electrical resistance is observed, see the black curve in Fig. 5. The increasing trend of the resistance slows down and eventually, a decrease is observed due to disappearing α/β interfaces. Dilatometry shows that the sample length ceases to grow at about 600 °C (see the black line in Fig. 7), and it even decreases in a short temperate range, see the negative derivative of the thermal expansion in Fig. 9. This means that the dissolution of the α phase, which has a large molar volume (Fig. 7), leads to shortening of the sample which has a stronger influence than the length increase due to thermal dilatation. The α dissolution is reflected also in the evolution of the lattice parameter of the β phase. Due to decreasing Nb content (Nb migrates back to regions where α disappeared), the lattice parameter of the β phase decreases, see Fig. 6. At the same time, the molar volume of the β phase remains much smaller than that of the α phase. This is another reason for the decrease of thermal expansion (Fig. 7). As the temperature increases, the thermal expansion rises again, but much slower than what would correspond only to thermal dilatation of a pure material without any phase transformations.

The β transus temperature could not be reliably determined in the temperature range of the employed experiments. In HEXRD, peaks belonging to the α phase can be discerned even for the highest reached temperature, 800 °C (see Fig. 1), even though the theoretical phase diagram predicts the β transus at 680 °C (Fig. 4). This may be caused by oxygen content in the alloy or the possibility that the surface of the sample was oxidized, locally increasing the β transus temperature. The other in-situ methods are not sufficiently sensitive to the β transus; the electrical resistance curve can show a change of the slope [36] but other experiments would need to be performed to determine the β-transus temperature unambiguously.

## 4. Conclusions

A unique combination of analytical methods was used to clarify the phase transformation sequence occurring in a metastable β Zr–12Nb alloy. HEXRD was measured in situ during linear heating simultaneously with dilatometry. Additionally, electrical resistance and DSC were measured with the same heating rate. The microstructure of several conditions heated up to selected temperatures and quenched was observed by TEM.

The most important findings of this research can be summarised as follows.

- During linear heating, two distinct bcc phases were observed in accordance with the Zr–Nb phase diagram. The initial solution treated condition consists of a metastable $\beta_{Zr}$ phase and nanometre-sized $\omega_{ath}$ particles. At about 300 °C the Nb-rich $\beta_{Nb}$ phase with a lower lattice parameter starts to precipitate and the original $\beta_{Zr}$ phase gradually disappears.
- Starting at approximately 250 °C, the weight fraction of the ω phase increases. At about 450 °C, the ω particles start to coarsen while their total weight fraction decreases. At 560 °C, the ω solvus was found. At this temperature, the remaining ω particles dissolve rapidly and α particles start to grow.
- The isothermal ω particles have a cuboidal shape which is caused by a large misfit of the β and ω lattices.

- Above the eutectoid temperature, the α phase gradually transforms back to the β phase.
- Phase transformation sequence in metastable β-Zr alloys is similar to their Ti-based counterparts; however, significant differences arise. Detailed understanding of phase transformations in these novel materials will facilitate their utilization in future applications.

## Declaration of competing interest

The authors declare that they have no known competing financial interests or personal relationships that could have appeared to influence the work reported in this paper.

## Acknowledgements

Financial support by the Czech Technological Agency, Czechia, under the project TK01030153 is gratefully acknowledged. Partial financial support by CSF project 21–18652 M is also gratefully acknowledged. A.V. and J.K. acknowledge project Grant schemes at Charles University, Czechia (reg. no. CZ.02.2.69/0.0/0.0/19_073/0016935). P.B.-V. acknowledges financial support from the Spanish Ministry of Science through the Ramón y Cajal grant RYC2020-029585-I. The annealing and structural analysis was performed in Materials Growth and Measurement Laboratory MGML (see: http://mgml.eu) which is supported within the program of Czech Research Infrastructures (project no. LM2018096).

## REFERENCES

[1] Weinberg AM. Phys Today 1993;46:70–1.
[2] Rickover HG, Geiger LD, Lustman B. History of the development of zirconium alloys for use in nuclear reactors, energy research and development administration. Washington, D.C. (USA): Div. of Naval Reactors; 1975.
[3] B. Cox. Uhlig's corrosion handbook. John Wiley & Sons, Ltd; 2011. p. 893–900.
[4] Mantripragada VP, Lecka-Czernik B, Ebraheim NA, Jayasuriya AC. J Biomed Mater Res 2013;101:3349–64.
[5] Duan Z, Yang H, Satoh Y, Murakami K, Kano S, Zhao Z, et al. Nucl Eng Des 2017;316:131–50.
[6] Azevedo CRF. –1962. Eng Fail Anal 2011;18:1943.
[7] Lemaignan C, Motta AT. Materials science and technology. John Wiley & Sons, Ltd; 2006.
[8] Whitmarsh CL. Review of ZIRCALOY-2 and ZIRCALOY-4 properties relevant to N.S. Savannah Reactor Design; 1962.
[9] Bethune MrsIT, Williams CD. J Nucl Mater 1969;29:129–32.
[10] Rogachev StanislavO, Nikulin SA, Rozhnov AB, Gorshenkov MV. Adv Eng Mater 2018;20:1800151.
[11] Ribis J, Doriot S, Onimus F. J Nucl Mater 2018;511:18–29.
[12] Gurovich BA, Frolov AS, Kuleshova EA, Maltsev DA, Safonov DV, Alekseeva EV. Mater Char 2019;150:22–30.
[13] Sabol G. J ASTM Int (JAI) 2005;2.
[14] Nikulina AV. Met Sci Heat Treat 2004;46:458–62.
[15] Garde A, Comstock R, Pan G, Baranwal R, Hallstadius L, Cook T, et al. Zirconium in the nuclear industry: 16th international symposium. 2012.
[16] Liang J, Yu H, Barry A, Corcoran EC, Balogh L, Daymond MR. J Alloys Compd 2017;716:7–12.
[17] Sattari M, Holt RA, Daymond MR. J Nucl Mater 2013;435:241–9.
[18] Ati ALVAC. ATI 15Mo Titanium alloy. Technical Data Sheet; 2014.
[19] Zháňal P, Harcuba P, Stráský J, Šmilauerová J, Beran P, Hansen TC, et al. Materials 2019;12:3570.
[20] Zháňal P, Harcuba P, Hájek M, Smola B, Stráský J, Šmilauerová J, et al. J Mater Sci 2018;53:837–45.
[21] Šmilauerová J, Janeček M, Harcuba P, Stráský J, Veselý J, Kužel R, et al. J Alloys Compd 2017;724.
[22] Barriobero-Vila P, Requena G, Warchomicka F, Stark A, Schell N, Buslaps T. J Mater Sci 2014;50.
[23] Barriobero-Vila P, Requena G, Schwarz S, Warchomicka F, Buslaps T. Acta Mater 2015;95:90–101.
[24] Aeby-Gautier E, Settefrati A, Bruneseaux F, Appolaire B, Denand B, Dehmas M, et al. J Alloys Compd 2013;577:S439–43.
[25] Boyer RR. Mater Sci Eng, A 1996;213:103–14.
[26] Bolcich JC, Peretti HA, Ahlers M. J Nucl Mater 1980;95:311–3.
[27] Marques FDS. Int J Mater Res 1978;69:157–62.
[28] Guo S, Zhang J, Shang Y, Zhang J, Meng Q, Cheng X, et al. J Alloys Compd 2018;745:234–9.
[29] Xia C, Feng Z, Liu S, Zhang X, Zhang B, Pan B, et al. Corrosion Sci 2017;127:39–44.
[30] Nie L, Zhan Y, Hu T, Chen X, Wang C. J Mech Behav Biomed Mater 2014;29:1–6.
[31] Chui P. Vacuum 2017;143:54–8.
[32] Suyalatu null, Kondo R, Tsutsumi Y, Doi H, Nomura N, Hanawa T. Acta Biomater 2011;7:4259–66.
[33] Kondo R, Nomura N, Suyalatu, Tsutsumi Y, Doi H, Hanawa T. Acta Biomater 2011;7:4278–84.
[34] Nomura N, Tanaka Y, Suyalatu, Kondo R, Doi H, Tsutsumi Y, et al. Mater Trans 2009;50:2466–72.
[35] Bartha K, Stráský J, Barriobero-Vila P, Šmilauerová J, Doležal P, Veselý J, et al. J Alloys Compd 2021;867:159027.
[36] Zháňal P, Harcuba P, Šmilauerová J, Stráský J, Janeček M, Smola B, et al. Acta Phys Pol, A 2015;128:779–82.
[37] Zháňal P, Harcuba P, Hájek M, Stráský J, Šmilauerová J, Veselý J, et al. J Appl Crystallogr 2019;52:1061–71.
[38] Abriata JP, Bolcich JC. Bulletin of Alloy Phase Diagrams 1982;3:34–44.
[39] Murray JL. Bulletin of Alloy Phase Diagrams 1981;2:185–92.
[40] De Fontaine D. Acta Metall 1970;18:275–9.
[41] Šmilauerová J, Harcuba P, Stráský J, Stráská J, Janeček M, Pospíšil J, et al. Acta Mater 2014;81:71–82.
[42] Šmilauerová J, Harcuba P, Kriegner D, Holý V. J Appl Crystallogr 2017;50:283–7.
[43] Schell N, King A, Beckmann F, Fischer T, Müller M, Schreyer A. Mater Sci Forum 2014;772:57–61.
[44] Staron P, Fischer T, Lippmann T, Stark A, Daneshpour S, Schnubel D, et al. Neutrons and synchrotron radiation in engineering materials science: from fundamentals to applications. second ed. 2017. p. 365–75.
[45] Hammersley AP. J Appl Crystallogr 2016;49:646–52.
[46] Rodríguez-Carvajal J. Phys B Condens Matter 1993;192:55–69.
[47] Aldridge SA, Cheadle BA. J Nucl Mater 1972;42:32–42.
[48] Rossiter PL. The electrical resistivity of metals and alloys. Cambridge University Press; 1991.
[49] Zháňal P, Václavová K, Hadzima B, Harcuba P, Stráský J, Janeček M, et al. Mater Sci Eng C 2016:886–92.
[50] Janeček M, Bartha K, Stráský J, Veselý J, Polyakova V, Semenova I. Defect Diffusion Forum 2018;385:206–11.
[51] Harcuba P, Šmilauerová J, Hájek M, Zháňal P, Čapek J. Proceedings of the 13th world conference on titanium. John Wiley & Sons, Ltd; 2016. p. 437–41.
[52] Williams JC, Blackburn MJ. 2352-5 Trans. Met. Soc. AIME Oct. 1969;245:245 (1969).